Journal of Magnetism and Magnetic Materials 475 (2019) 316–326

Contents lists available at ScienceDirect

Journal of Magnetism and Magnetic Materials

journal homepage: www.elsevier.com/locate/jmmm

Research articles

Poly-L-lysine designed magnetic nanoparticles for combined hyperthermia, magnetic resonance imaging and cancer cell detection

M. Kubovcikova[a], M. Koneracka[a,*], O. Strbak[b], M. Molcan[a], V. Zavisova[a], I. Antal[a], I. Khmara[a,d], D. Lucanska[a,e], L. Tomco[f], M. Barathova[c], M. Zatovicova[c], D. Dobrota[g], S. Pastorekova[c], P. Kopcansky[a]

[a] Institute of Experimental Physics, Slovak Academy of Sciences, Watsonova 47, Kosice, Slovakia
[b] Biomedical Center Martin, Jessenius Faculty of Medicine in Martin, Comenius University in Bratislava, Mala Hora 4, 036 01 Martin, Slovakia
[c] Institute of Virology, Biomedical Research Center, Slovak Academy of Sciences, Dubravska cesta 9, Bratislava, Slovakia
[d] Pavol Jozef Safarik University, Faculty of Science, Park Angelinum 9, Kosice, Slovakia
[e] Technical University, Faculty of Electrical Engineering and Informatics, Letna 9, Kosice, Slovakia
[f] Technical University, Faculty of Aeronautics, Rampova 7, Kosice, Slovakia
[g] Department of Medical Biochemistry, Jessenius Faculty of Medicine in Martin, Comenius University in Bratislava, Mala Hora 4, 036 01 Martin, Slovakia

ARTICLE INFO

Keywords:
Magnetic nanoparticles
Poly-L-lysine
Magnetic hyperthermia
Antibody
MRI
Relaxivity

ABSTRACT

The aim of this study was to test the suitability of poly-L-lysine coated magnetic nanoparticles for combined magnetic hyperthermia and magnetic resonance imaging (MRI) to unify the therapeutic and diagnostic approach. For this purpose, we have synthetized magnetic iron oxide (Fe_3O_4) nanoparticles of core diameter ~10 nm and modified with Poly-L-lysine (PLL) to stabilize the particles and improve their biocompatibility. These modified nanoparticles (MFPLL) were tested for magnetic hyperthermia suitability by calorimetric measurements. Based on the estimated heating rates the specific absorption rates (SAR) for MFPLL particles were calculated. The SAR values of MFPLL particles were about 14–15 Wg^{-1} at frequency 190 kHz and applied field ~8 kAm^{-1}. In the MRI parametric mapping measurements we demonstrated the significant effect of MFPLL on transversal relaxation time T_2 with the relaxivity r_2 equal to 487.94 $mM^{-1}s^{-1}$. The combination of the heating properties with the cytotoxic activities of MFPLL and MRI parameters holds great promise for the future development of targeted synergistic cancer treatment. Furthermore, as our previous results confirmed the cytotoxic activities of MFPLL in a cell type-dependent manner and the binding to cells expressing carbonic anhydrase (CA IX) when conjugated with the CA IX-specific antibody we have studied the antibody conjugated MFPLL nanoparticles in 3D spheroidal culture.

1. Introduction

Magnetic nanoparticles (MNPs) appear to be a very promising material for use in biomedicine. A great advantage of MNPs is their size, which is less or comparable to cells (10–100 μm), viruses (20–450 nm), proteins (5–50 nm) or genes (width 2 nm, length 10–100 nm). Such small dimensions allow good tissue diffusion and they are an advantage for the distribution of nanoparticles as close as possible to the site of biological interest. Their magnetic properties make MNPs manipulation possible by applying an external magnetic field, which opens up a large scale of their use. MNPs thus find utilization in many medical branches such as cell labelling, drug delivery, magnetic resonance imaging (MRI), magnetic hyperthermia for cancer therapy and many others. Hyperthermic cancer treatment kills cancer cells by increasing their temperature to a therapeutic temperature range of 42–46 °C [1]. This approach can destroy tumors with minimal damage to healthy tissues, and thus reduces or eliminates negative side effects of drugs. As far as the scale of its use goes, it is one of the most important thermo-therapeutic methods where MNPs are injected directly into tumor and the next step is the application of a high frequency alternating magnetic field with a frequency of 50 kHz–1.2 MHz. Losses at reversal magnetizing of MNPs cause local heating and subsequent thermal destruction of the tumor. One of many areas of possible use of nanoparticles is diagnostic medicine as well. MNPs are widely used in MRI. The principle of MRI is the nuclear magnetic resonance of hydrogen atoms. In order to get images of sufficient quality, it is usually necessary to

* Corresponding author.
E-mail address: konerack@saske.sk (M. Koneracka).

https://doi.org/10.1016/j.jmmm.2018.11.027
Received 15 June 2018; Received in revised form 24 September 2018; Accepted 4 November 2018
Available online 14 November 2018
0304-8853/

increase their contrast. For this purpose contrast agents are utilized. To be used as contrast agent, MNPs should exhibit high saturation magnetization and be functionalized with ligands ensuring optimal diffusion of water molecules around the magnetic core [2]. Sufficiently high saturation magnetization and relaxivity *r* are important parameters for the successful use of a contrast agent.

Numerous *in vitro* experiments were conducted with promising results. The issue that makes the *in vivo* applications of MNPs a difficult task is biocompatibility and stability under physiological conditions. Therefore, a considerable effort in MNPs development is put into preparing nanoparticles with added functionalities that could be used for therapy and for imaging. In addition, the functionalization is a necessary prevention of aggregation, and at the same time a means of ensuring the biocompatibility and nontoxicity of nanoparticles used in medicine. Another reason for the surface functionalization of MNPs is to monitor the effect of the functionalized shell of MNPs on protein interactions, i.e. a process making MNPs get into a biological fluid (e.g., blood, plasma) or into a culture medium where they are surrounded by the proteins. Last but not least, functionalized MNPs are also useful in conjugating antibodies with specific affinity to tumor cells [3].

The discovery of antigens overexpressed on the surface of cancer cells suggests that certain monoclonal antibodies (MAbs) could distinguish malignant tumors from normal tissues and could be used for selective targeting of tumor cells [4]. The first step in developing a targeted cancer therapy is a generation of an antibody that binds to a receptor which is either tumor-specific or sufficiently overexpressed in tumors to provide targeting selectivity. Carbonic anhydrase IX (CA IX), one of the best markers of tumor hypoxia and a prognostic indicator of cancer, is suitable as a target for cancer therapy due to its cell surface localization and functional involvement in cancer [5]. Interest in the development of MAbs conjugated with radionuclides, drugs, toxins and magnetic nanoparticles has recently been revitalized. Recent clinical studies show that monoclonal antibodies that are specific for tumor-associated antigens and capable to induce a receptor-mediated internalization can represent efficient tools for immunotherapy of tumors. Out of the set of monoclonal antibodies against the extracellular domains of CA IX [6], only the VII/20 MAb was capable of internalization [7].

Detection of tumor cells mediated by antibodies in combination with MRI and hyperthermia represents a significant advance in cancer diseases treatment and a substantial improvement in survival of oncological patients.

The presented work builds up on the results achieved and described in the work [3]. Our aim is the study of the suitability of Poly-L-lysine modified magnetic nanoparticles (MFPLL) in MRI and magnetic hyperthermia. The next fundamental goal is the conjugation of a selected specific antibody VII/20, capable of internalization, to pre-modified magnetic nanoparticles. Finally, 3D model of MNPs accumulation in tumor spheroids for better prediction of selectivity and toxicity *in vivo* is investigated.

2. Materials and methods

2.1. Materials

Poly-L-lysine (PLL) hydrobromide $((C_6H_{12}N_2O)_n$. HBr; Mw = 150,000–300,000 g/moL), ferric chloride hexahydrate ($FeCl_3{\cdot}6H_2O$), ferrous sulphate heptahydrate ($FeSO_4{\cdot}7H_2O$), and ammonium hydroxide (NH_4OH) were purchased from Sigma-Aldrich. All solutions were prepared using ultrapure water.

2.2. Preparation of magnetic nanoparticles

PLL modified magnetic nanoparticles were prepared in 3 steps according to the procedure described in [3]. Briefly, at the first stage magnetite nanoparticles were precipitated from an aqueous solution of Fe(2+) and Fe(3+) ions while ammonium hydroxide was dropwise added. The precipitate was washed with ultrapure water and agitated with the immersed probe of a sonicator (BRANSON – Model 450) for 5 min at 70% of maximum power (280 W) in the water bath. In the next step, a modification of magnetite nanoparticles with PLL was done. The suspension of nanoparticles was mixed with PLL solution (0.1%) at the theoretical PLL/Fe_3O_4 weight ratio 1 (corresponding to PLL loading 0.25 mg/mL). The mixture was sonicated for 5 min at 70% power in the ice bath. Afterwards, the samples were subjected to ultracentrifugation at 44,000 g for 2 h at 4 °C. The supernatants were removed and the sediments were thoroughly dispersed in ultrapure water and collected to prepare final MFPLL sample with the magnetite and PLL concentrations of 18.5 and 3.6 mg/mL, respectively.

2.3. Characterization of magnetic nanoparticles

The prepared samples were characterized in terms of size distribution, stability and magnetic properties. Zetasizer Nano ZS (Malvern, UK) was used to obtain particle size distribution based on the Brownian motion and zeta potential values. Transmission electron microscope JEOL-TEM 2100F (TEM) operated at 200 kV and scanning electron microscope JEOL 7000F (SEM) were used to acquire electron micrographs for size and shape description. MPMS 5XL magnetometer (Quantum Design, Inc.) was used to carry out magnetic characterization including magnetization loop and AC magnetic susceptibility measurements.

2.4. Magnetic hyperthermia measurements

Magnetic hyperthermia (calorimetric) measurements were conducted to find out the response of magnetic nanoparticles to an applied alternating magnetic field (AMF). An AMF was generated by a home-made setup. A high-frequency sinusoidal signal (190 kHz) was amplified by an AL-600-HF-A power amplifier (Amp-Line; West Nyack, NY, USA) connected to the LC circuit. The AMF (up to 7874 A/m) was generated in the middle of the coil cavity, where a glass vial with a magnetic colloid (1 mL) was placed. An FPIHR module equipped with the fiber optic temperature sensor (immersed in the glass vial), model FOTL-SD-C1-F2-M2-R5-SCAI (FISO Technologies; Québec, Canada) was used for temperature recording in time at a given frequency and applied magnetic field. The accuracy of temperature measurements was ± 0.1 K. The used setup and AMF generation was previously described in [8,9].

2.5. MRI parametric mapping

MRI relaxivity measurements were performed at 7 T BioSpec Bruker system. Three different protocols were used for T_1, T_2, and T_2^* parametric mapping: (1) T_1 mapping – Rapid Acquisition with Refocused Echoes (RARE) pulse sequence, with repetition time TR = 5500, 3000, 1500, 800, 400, 200 ms, echo time TE = 7 ms, (2) T_2 mapping – Multi-Slice Multi-Echo (MSME) pulse sequence, with repetition time TR = 2000 ms, starting echo time TE = 8 ms, spacing = 8 ms, 25 images, and (3) T_2^* mapping - Multi Gradient Echo (MGE) pulse sequence, with repetition time TR = 800 ms, starting echo time TE = 5 ms, spacing = 10 ms, 10 images.

Prior to relaxivity measurement, the MFPLL sample was diluted with a concentration gradient of magnetite as follows: 2.5, 5, 7.5, 10, 12.5, 15, 17.5 and 20 μg/mL. The PLL without magnetite was used as the reference sample. The signal intensity of the PLL without magnetite (I_0), and with magnetite concentration gradient ($I_{1\text{-}8}$) were acquired and evaluated. Subsequently the longitudinal and transversal relaxation times (T_1, T_2, T_2^*) were determined by fitting with the following functions:

$$M(t) = A + M_0 * (1 - exp(t/T_1)) \quad (1)$$

$$y = A + C * exp(-t/T_2) \quad (2)$$

where M_0 is the equilibrium magnetization, A is the absolute bias, T_1 is the longitudinal recovery time, C is the signal intensity, and T_2 is the transversal relaxation time.

The value of T_2 relaxation time is only influenced by atomic/molecular interactions, while T_2^* value reflects atomic/molecular interactions as well as the main magnetic field (B_0) inhomogeneities. Afterwards, the relative contrast (RC), transversal and longitudinal relaxation rate (R_1, R_2, R_2^*), and relaxivity (r_1, r_2, r_2^*) were calculated and evaluated. The relative contrast of magnetite nanoparticles as a negative contrast agent ($I_0 > I$) is defined as follows:

$$RC = (I - I_0)/I_0 \quad (3)$$

where I_0 is the signal intensity without magnetite particles, and I represents the signal intensity with magnetite nanoparticles. The transversal relaxation rate (R) is inverse to the relaxation time (T):

$$R_n = 1/T_n (n = 1, 2) \quad (4)$$

The change in transverse relation rate R_n is defined as the relaxivity of the magnetic nanoparticles (contrast agent):

$$r_n = (R_n - R_n^0)/C (n = 1, 2) \quad (5)$$

where R_n^0 is the relaxation rate in the absence of magnetic particles, R_n represents the relaxation rate in the presence of magnetic particles, and C is the particle's concentration. For data processing the following software tools were employed: Paravision "Image Sequence Analysis" tool (Bruker, Germany), and Matlab R2011b (Mathworks Inc., Natic USA).

2.6. Colloidal stability under different condition

Polydispersity, hydrodynamic diameter and zeta potential measurements were performed in order to evaluate the colloidal stability of both MFPLL and Ab-conjugated nanoparticles (Ab-MFPLL) in phosphate buffered saline (PBS) in the pH range from 2 to 12. Moreover, a long-term stability of amino modified MNPs without and with conjugated antibody in cell culture medium (10% FBS in DMEM) was studied. For that purpose, the size distributions were measured at specific intervals after initial time $t = 0$. Measurements were made at $t \approx 0.5$, 1.2 up to 74 h at 25 and 37 °C using dynamic light scattering apparatus. The values of hydrodynamic diameter and the polydispersity index were recorded and processed.

2.7. Antibody conjugation to MFPLL

Conjugation of monoclonal antibody VII/20 (Ab) to MFPLL was carried out at room temperature in PBS. A 30 µL of MFPLL suspension (18.5 mg Fe_3O_4/mL in PBS) and 1 mL of antibody solution (0.146 mg Ab/mL) were mixed together to a final volume of 3 mL in PBS, and shaken overnight at 25 °C. The antibody-conjugated particles (Ab-MFPLL) were washed with PBS buffer by magnetic decantation. Washings containing unconjugated antibody were analyzed using a UV/VIS spectrophotometer at λ_{MAX} = 591 nm by Bradford dye method. The amount of antibody conjugated to the particles was calculated from the difference between the antibody used for conjugation and the antibody present in the washings. Different reaction parameters like magnetite/antibody weight ratio, magnetite concentration and antibody concentration were optimized to prepare stable Ab-conjugated sample with maximum amount of antibody conjugation.

2.8. Cellular uptake study in 3D multicellular spheroidal cell culture

2.8.1. Spheroids formation and treatment with MFPLL

Spheroids formation was induced in hanging drops. 2000 of HT29 colorectal cancer cells were cultivated in 20 µL drop of high glucose DMEM medium (supplemented with 10% fetal calf serum, BioWhitttaker, Verviers, Belgium) hanging from the lid of culture dish for 5 days to allow to form cell aggregates. The aggregates were then transferred to a non-adherent Petri dish. The spheroids were cultivated in suspension for 5 days in a humidified atmosphere with 5% CO_2 at 37 °C. Before fixation, the spheroids were treated with the antibody conjugated to MFPLL or with non-conjugated MFPLL for 24 h at 37 °C and 5% CO_2.

2.8.2. Fixation of spheroids and immunohistochemistry

Serial sections (4 µm) of Carnoýs fluid fixed and paraffin embedded HT29 spheroids were stained for binding of Ab-MFPLL and for CA IX protein using EnVision + System HRP DAB (DAKO). Briefly, endogenous peroxidase activity was quenched by incubating the specimens for 5 min with Peroxidase block (part of the kit). Then sections were incubated with primary anti-CA IX monoclonal antibody diluted 1:100 for 1 h in humidity chamber, washed and followed by incubation with the labelled polymer anti-mouse HRP (part of the kit) for 30 min in humidity chamber. Staining was completed by incubation with 3,3′-diaminobenzidine (DAB) + substrate-chromogen resulting in a brown-colored precipitate at the antigen site. For detection of specific binding of Ab-MFPLL conjugate the polymer anti-mouse HRP antibody only, without incubation with primary antibody, was used. After the immunostaining, the sections were counterstained with hematoxylin and mounted with Entellan Neu mounting medium (Merck, Darmstadt, Germany). The sections were finally examined and imaged with a Zeiss Axioskop 40 microscope (Carl Zeiss, Gottingen, Germany).

3. Results and discussion

3.1. Samples characterization

The synthetized amino modified MNPs were characterized in detail in our previous studies by various techniques [3,10]. In this paper, we added additional results of microscopy evaluation, as microscopy

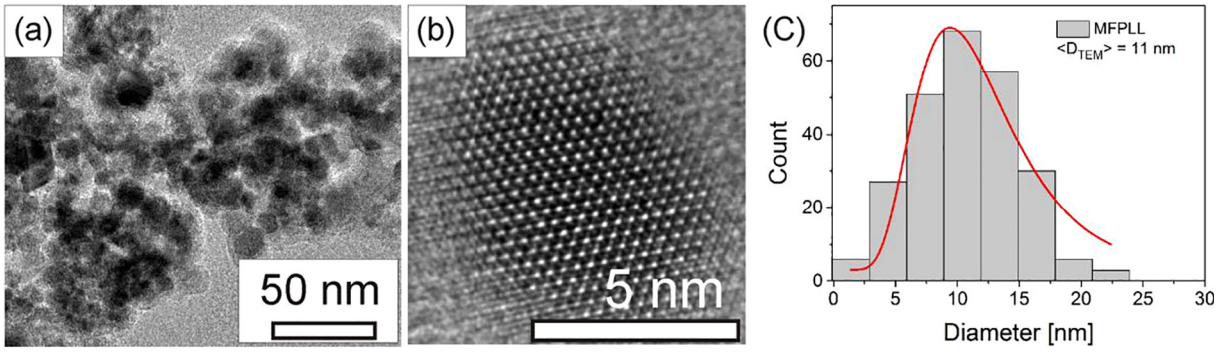

Fig. 1. General view of the PLL modified iron oxide MNPs by TEM (a); HRTEM picture of a particle displaying lattice (b), and size distribution histogram (c).

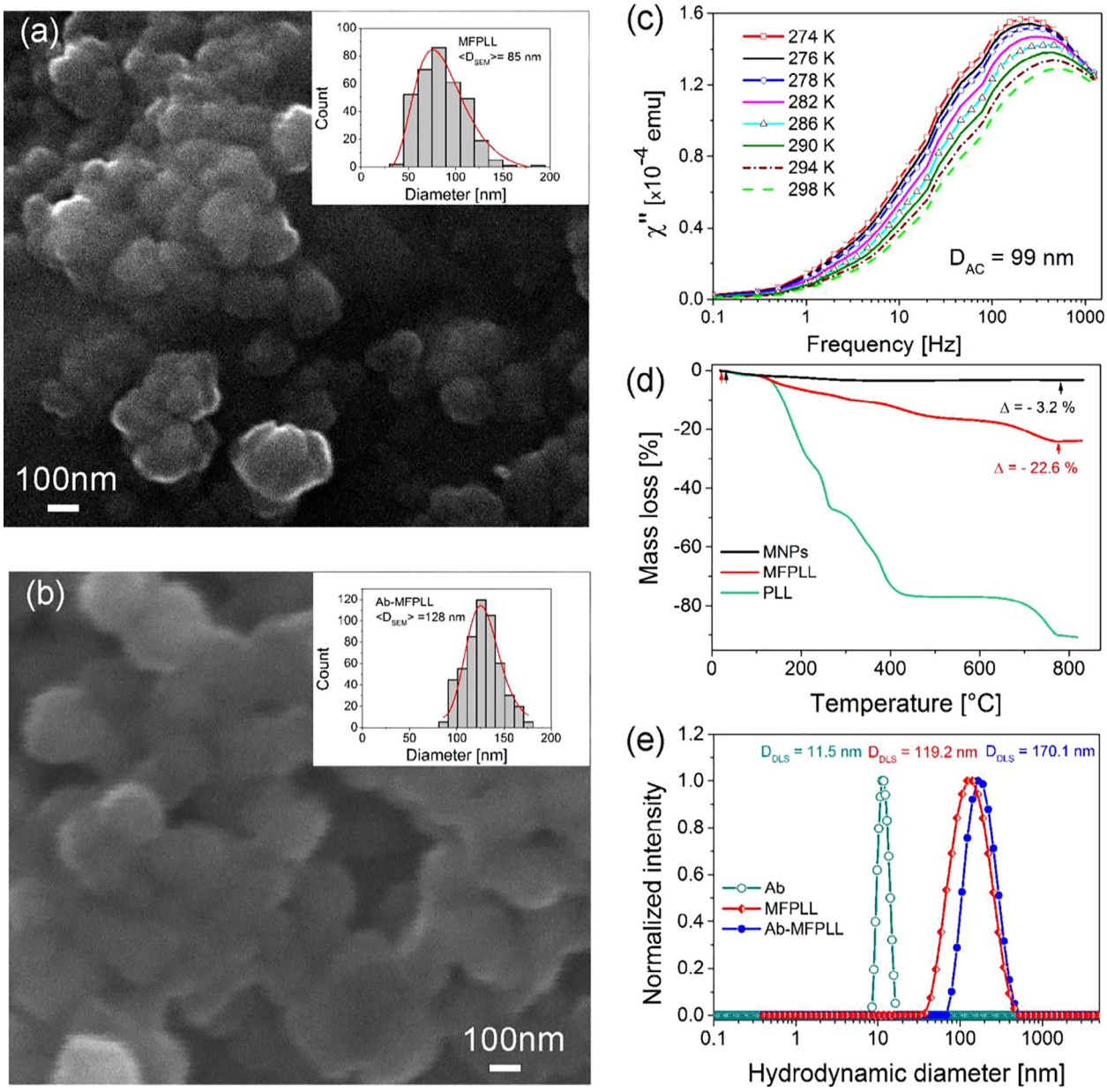

Fig. 2. SEM images of MFPLL (a) and Ab-MFPLL (b). AC susceptibility measurements of MFPLL (c), TGA curves of MFPLL (d) and DLS size distributions (e).

allows us to "really" see the particles and evaluate their range of size and shape. TEM gives us not only a general view of the PLL modified MNPs but also this technique is suitable to determine the average particle size (Fig. 1a, c). As shown in the TEM images, PLL modified MNPs exhibited diameters ranging from 2 to 23 nm with the mean size of approximately 11 nm (Fig. 1c). To evaluate the MNPs size distribution from TEM images, the software Image J was used. Fig. 1b displays high resolution electron microscopy (HRTEM) image of a single nanoparticle.

The high resolution TEM image allowed obtaining a direct resolution of the atomic columns of the nanoparticle. Shape and morphology of the nanoparticles observed by SEM revealed nearly spherical shape of prepared samples with mean diameter D_{SEM} = 85 and 128 nm for MFPLL and Ab-MFPLL (Fig. 2a,b). These results were close to results from DLS measurements. The hydrodynamic diameter of MFPLL after Ab-conjugation increased from 119.2 nm to 170.1 nm (Fig. 2e). The difference in size agrees with the D_{HYDR} of pure Ab and gives us information about the adsorbed Ab layer thickness.

The zeta potential value of ~ +50 mV is a sign of good colloidal stability of prepared samples. For quantification of magnetic nanoparticles coating, TGA measurement was used as well. The TGA scans of bare MNPs, pure PLL and MFPLL are depicted in Fig. 2d. The data demonstrate that the coating on the nanoparticle was measured to be 19.4% of the total mass (red curve). This represents only 0.129 mg PLL per 1 mg of magnetite. Field dependent magnetization measurements performed at 290 K (data not shown) indicated superparamagnetic behavior of the samples. Frequency dependence of the AC susceptibility imaginary part measured at different temperatures was used for hydrodynamic diameter calculation of MFPLL (Fig. 2c). The corresponding hydrodynamic diameter value of 99 nm was in good agreement with the values obtained by other methods.

3.2. Magnetic hyperthermia

With the aim to verify the Fe_3O_4 concentration effect on heating characteristics of our samples the set of five MFPLL samples with concentrations in the range from 2.5 to 11.3 mg/mL was tested. Time evolution of temperature rise for MFPLL sample with the concentration

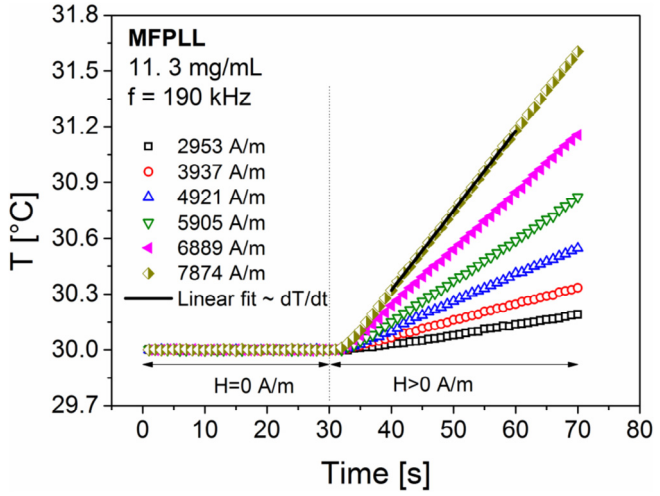

Fig. 3. Time evolution of temperature rises in MFPLL sample with the concentration of 11.3 mg/mL as a function of the applied alternating magnetic field strength amplitude H at frequency f = 190 kHz.

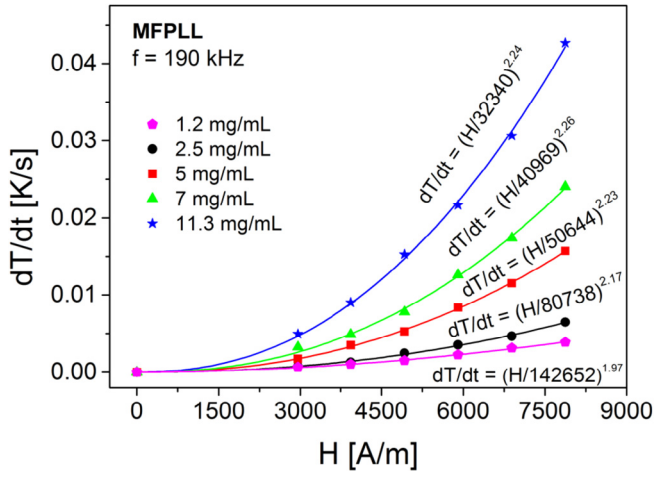

Fig. 4. Dependence of $(dT/dt)_{t=0}$ on the applied alternating magnetic field strength amplitude H at a frequency f = 190 kHz for MFPLL sample.

11.3 mg/mL as a function of the applied AMF with field strength amplitude H at frequency f = 190 kHz is shown in Fig. 3. The initial part of temperature dependence (up to 30 s) at T = 30 °C indicates a temperature stability of the sample at H = 0 A/m. Once the AMF H had been applied (in t = 30 s, for a period 40 s) the temperature rise was apparent instantly. With increasing AMF H the dynamics of the temperature increase (slope ~ dT/dt) became much more significant as well. The dT/dt for all MFPLL concentrations at each of the applied AMF intensity H was estimated as a linear fit of the temperature vs. time dependences in the range from 40 to 60 s. The obtained heating rates $\Delta T/\Delta t$ were subsequently plotted as a function of the AMF intensity (Fig. 4). The curves represent experimental data fitted by function $dT/dt = (H/a)^n$, where a and n are fitting parameters [9,11]. The observed dependences are associated with the energy losses contribution from relaxation processes described by Brownian or Néel mechanisms [12,13]. From dT/dt dependencies the specific absorption rate (SAR) values were estimated as the amount of heat released by a unit weight of the material per unit of time during exposure to an oscillating magnetic field of a given frequency and field strength [9,14]. The obtained values (W/g) were normalized to an effective amount of magnetite in the colloid and calculated according the following equation:

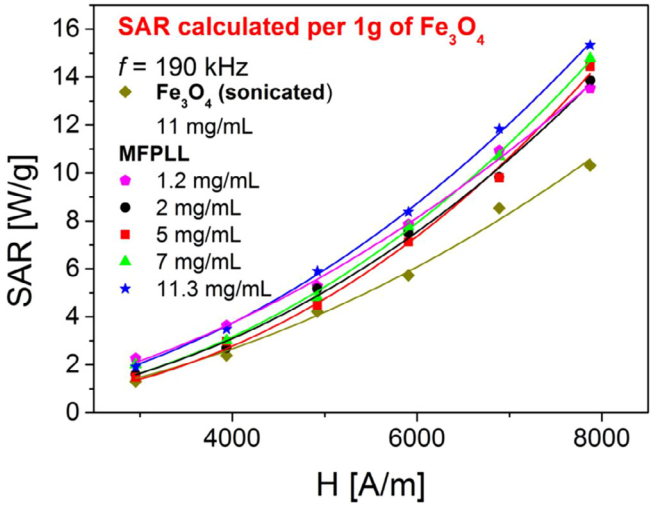

Fig. 5. SAR dependence of non-covered Fe_3O_4 and MFPLL particles measured for various sample concentrations and recalculated per 1 g of Fe_3O_4 at the frequency f = 190 kHz and applied field H up to ~8 kA/m.

$$SAR = \frac{C_p \rho_S}{m}\left(\frac{dT}{dt}\right)\left[\frac{\mathrm{W}}{g}\right]$$

where Cp (4.18 J/K.g) and ρ_S (1016 kg/m^3) are the specific heat and density of the sample, respectively, and m is the mass of magnetite per unit volume of the colloid. The SAR values of the MFPLL samples at H up to ~8 kA/m and f = 190 kHz are presented in Fig. 5. Calculated SAR values at the highest applied magnetic field (7.8 kA/m) reached approx. ~ 14–15 W/g. The values resulting from the conditions mentioned above are relatively low but still acceptable for a follow-up study with the aim to maximize them and test the sample in applications where the threat of patient's overheating exists. Comparable SAR values were obtained by Illés et al. [15], where 17.44 W/g at 329 kHz, 13.13 kA/m was measured for magnetite nanoparticles coated by P (PEGMA-AA) copolymer. Kolenko et al. [16] measured for magnetite nanoparticles functionalized by polyacrylic acid at 300 kHz and 12 kA/m SAR values ~46 W/g. For example Rodrigues et al. [17] measured SAR just 6.4 W/g at 70 kHz, 1.6 kA/m for Pluronic® coated magnetite nanoparticles. In general, according to Hergt et al. [18] commonly available iron oxide ferrofluids show the power losses below about 100 W/g, only in a few special cases (for instance, in case of magnetosomes) SAR experimental values exceeding 500 W/g up to about 1000 W/g were found. These results were also compared with a non-modified sample that was partially stabilized by sonication before the experiment. In this case, the SAR value was decreased to approx. 10 W/g. The lower SAR value can be attributed to the absence of PLL coating component that provides long-term stability of the particles in the colloid. This is the reason why the heating rate is lower, which is ultimately reflected in lower SAR value. To demonstrate obvious temperature increase in time the sample with a concentration of magnetite 21.3 mg/mL at two selected field intensities was tested (Fig. 6).

The starting temperature before the measurement was 30 °C. The lower field intensities were chosen to avoid the parasitic heat contribution from winding for a longer measurement time. Anyway the increase in temperature at 4.5 kA/m and t = 135 s was almost 20 °C.

3.3. MRI parametric mapping

The MFPLL were also examined in order to investigate the MRI contrast properties. The aim was to find the longitudinal (r_1) and transversal relaxivity (r_2) of nanoparticles and to verify their contrast properties. In general, the magnetite nanoparticles themselves exhibit the properties referred as a "negative contrast agent", producing such

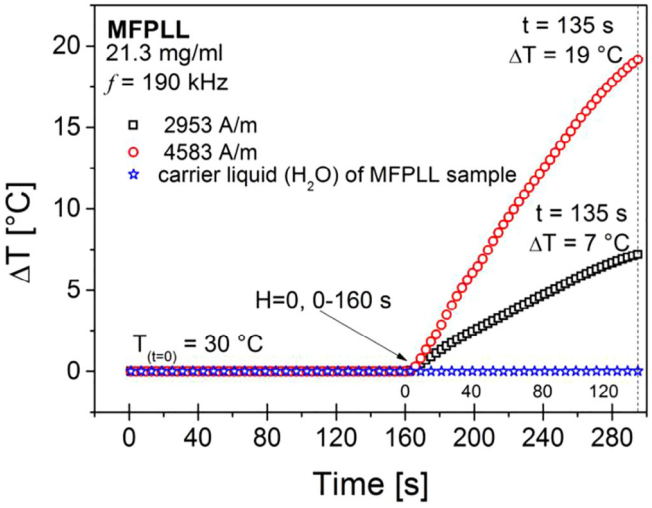

Fig. 6. Time evolution of temperature rises in MFPLL sample with the high concentration of 21.3 mg/mL as a function of the applied AMF with strength amplitude H at frequency $f = 190$ kHz. Blue line represents H_2O in AMF (4583 A/m), where temperature increase was not observed. (For interpretation of the references to colour in this figure legend, the reader is referred to the web version of this article.)

the MRI signal decrease (so called a hypointensive artifact) [19]. However, the size change of magnetic nanoparticles due to surface modification affects also relaxation time, and relaxivity [19,20]. For relaxivity measurements, the MFPLL were diluted to form the concentration gradient of magnetite. The prepared samples were measured with relaxation time-mapping pulse sequences (RARE, MSME, MGE) to obtain the signal intensity (I_0, I), and the relaxation time (T_1, T_2, T_2^*) values.

The contrast of samples and the relaxation time T_1 acquired with T_1-mapping RARE pulse sequence are shown in Fig. 7. The signal intensity (Fig. 7a,b) and the relaxation time T_1 (Fig. 7c) decrease, with the increasing concentration of magnetite, is clearly visible. The only exception is the lowest concentration of magnetite (2.5 μg/mL) (Fig. 7c), where the increase in relaxation time T_1 is observed. It is a typical feature of positive contrast agents that is, however, observed under specific conditions also in negative contrast agents. The specific conditions include size and concentration of magnetite nanoparticles [19]. The longitudinal relaxivity r_1 was obtained by linear fitting of the longitudinal relaxation rate R_1 and is equal to 1.81 $mM^{-1}s^{-1}$ (Fig. 7d).

In Fig. 8a,b is shown the contrast decrease caused by the T_2-mapping MSME pulse sequence. It is accompanied by the sharp shortening of the transversal relaxation time T_2 (Fig. 8c) in comparison with longitudinal relaxation time T_1 (Fig. 7c). Along with the curve patterns of the relative contrast in Fig. 7b and 8b, it indicates the prevailing effect of the MFPLL on the transversal relaxation time T_2. Fig. 8d shows the linear fit of the transversal relaxation rate R_2, with determined

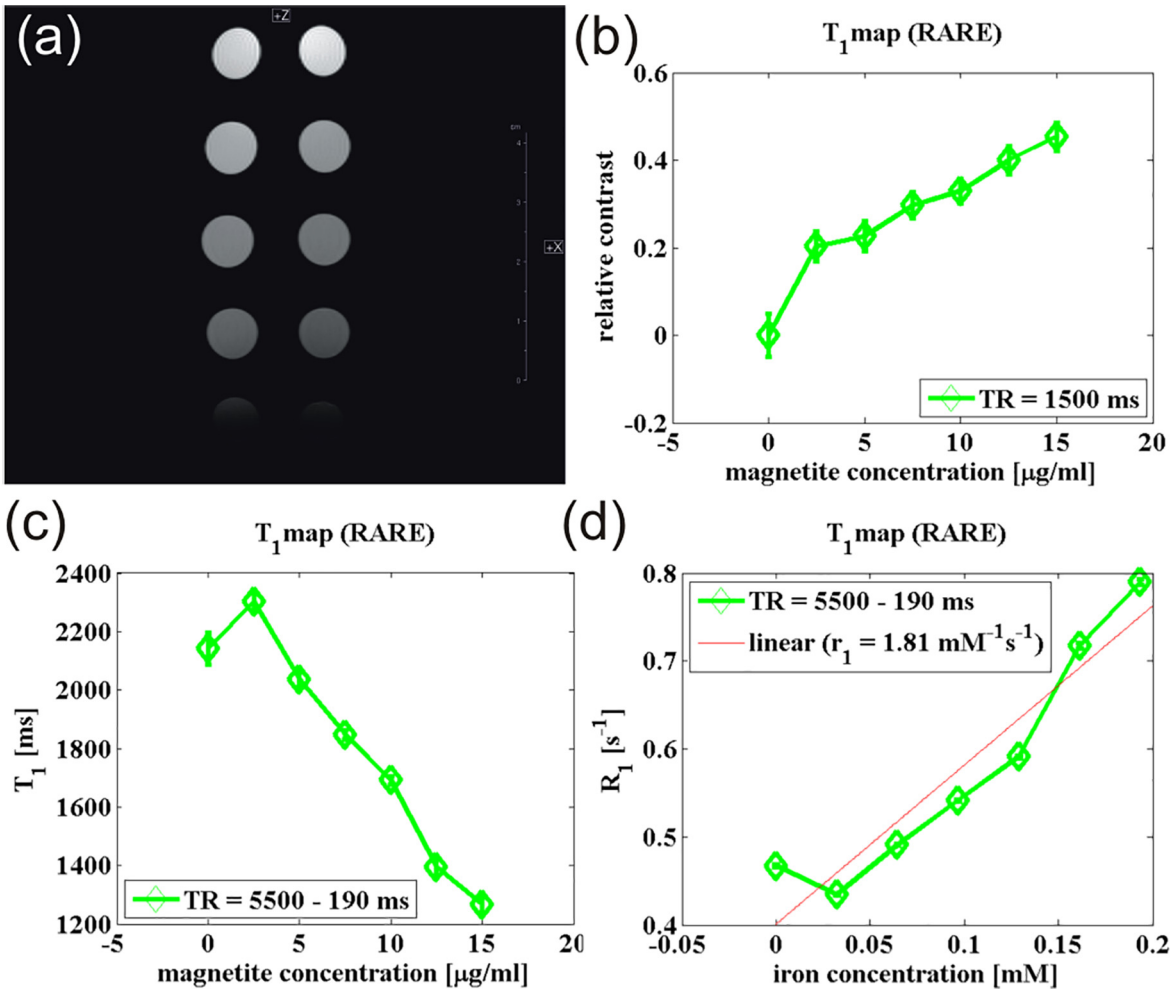

Fig. 7. Longitudinal relaxation time mapping of the MFPLL with T_1-mapping RARE pulse sequence. (a) The signal intensity. (b) The relative contrast depending on the magnetite concentration. (c) The relaxation time T_1 depending on the magnetite concentration. (d) The relaxation rate $R1$ depending on the magnetite concentration. Calculated relaxivity $r_1 = 1.81\ mM^{-1}s^{-1}$.

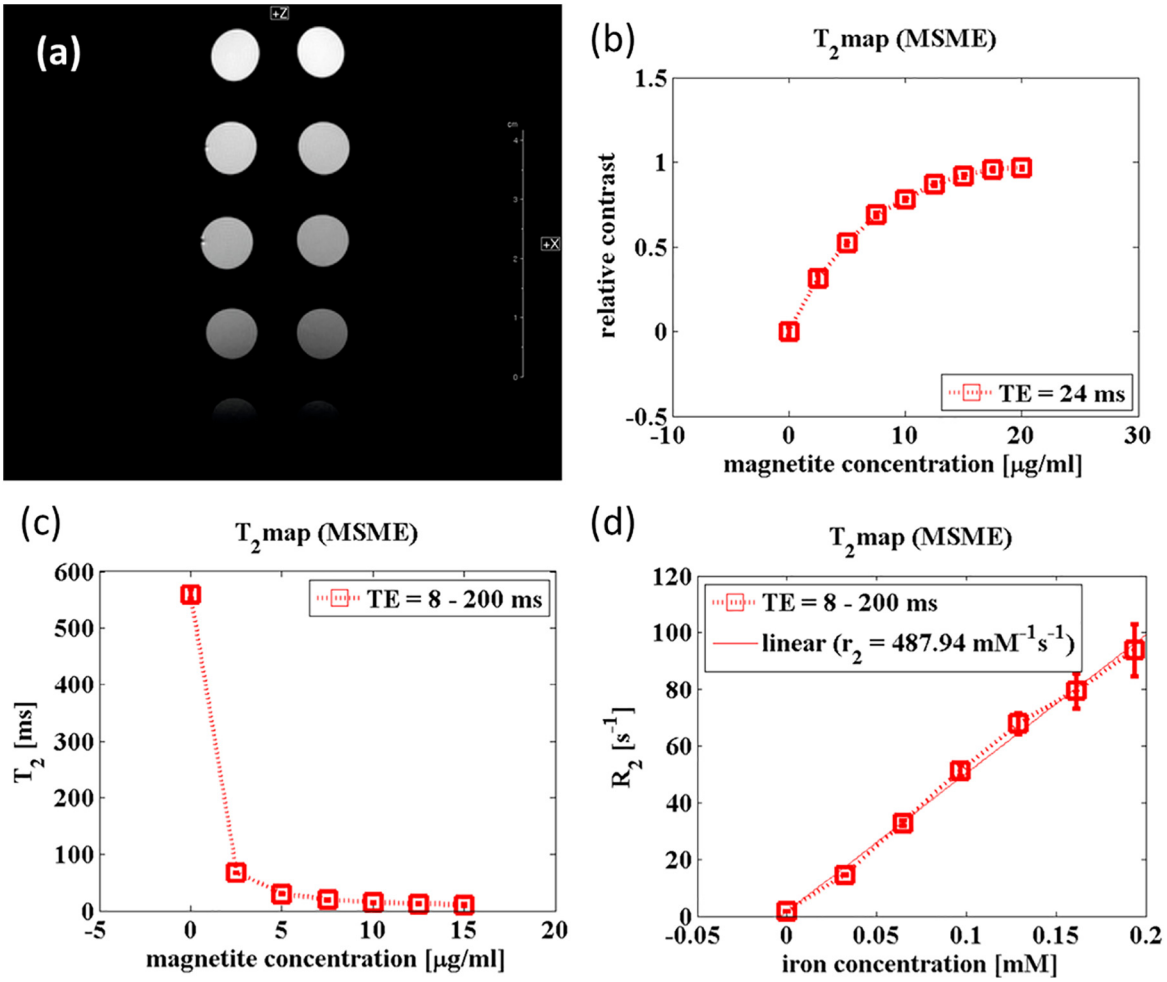

Fig. 8. Transversal relaxation time mapping of the poly-L-lysine modified magnetic nanoparticles with T_2-mapping MSME pulse sequence. (a) The signal intensity. (b) The relative contrast depending on the magnetite concentration. (c) The relaxation time T_2 depending on the magnetite concentration. (d) The relaxation rate R_2 depending on the magnetite concentration. Calculated relaxivity r_2 = 487.94 $mM^{-1} s^{-1}$.

relaxivity value r_2 equal to 487.94 $mM^{-1} s^{-1}$. It is a quite high value and together with ratio r_2/r_1 equal to 270 proves the significantly prevailing effect of the MFPLL nanoparticles on the transversal relaxation time T_2. These findings demonstrate the potential usefulness of the MFPLL as a negative contrast agent for MRI biomedical applications. Moreover, their transversal relaxivity r_2 significantly exceeds the transversal relaxivity of clinically used iron-based contrast agents: Feridex r_2 = 120 $mM^{-1} s^{-1}$, Resovist r_2 = 186 $mM^{-1} s^{-1}$, Combidex r_2 = 65 $mM^{-1} s^{-1}$ [14]. The T_2-mapping MSME protocol is not sensitive to magnetic field inhomogeneities produced by magnetite nanoparticles. It shows only the pure molecular interactions that affect the relaxation time. On the other hand, the T_2^*-mapping MGE pulse sequence reveals also image distortions caused by main field inhomogeneities produced by magnetic nanoparticles. This is visible in Fig. 9 that shows the relative contrast, relaxation time T_2^*, and relaxation rate R_2^* of the MFPLL. The T_2^*-map data are characteristic for their narrower signal decrease (Fig. 9b) and lower (or equal) value of relaxation time T_2^* (Fig. 9c) compared to the relaxation time T_2. The relaxivity value r_2^* is equal to 604.65 $mM^{-1} s^{-1}$ (Fig. 9d). This definitely confirms the potential of the PLL modified magnetic nanoparticles as a negative contrast agent in biomedical applications.

3.4. Antibody conjugation to MFPLL

In order to conjugate a specific monoclonal antibody that could be used for cancer cell detection and targeting, the amino modified MNPs were conjugated with VII/20 antibody. Several samples with various Ab/Fe_3O_4 weight ratio were prepared and quantified in terms of finding out the optimal weight ratio of Ab/Fe_3O_4 at maximum extend of Ab immobilization. The maximum extent of the coating was achieved at the input Ab/Fe_3O_4 weight ratio = 1/3. The spectrophotometric determination of the iron concentration of the Ab-MFPLL showed a concentration of 5.5 mg/mL. The amount of conjugated VII/20 antibody was determined with a Bradford dye method and it was found to be 200 μg of antibody per mg of magnetite. Both non-conjugated and Ab-conjugated MFPLL were characterized by DLS to make sure that the monodispersed and stable conjugated NPs were formed. An increase in the hydrodynamic diameters (see Fig. 2e) without major changes in the polydispersity index (PDI) for conjugated sample indicates the formation of Ab-conjugated MFPLL.

3.5. Stability evaluation of MFPLL and Ab-MFPLL

Samples' stability is a crucial factor affecting their further use. As the zeta potential is recognized as a good colloidal stability indicator, we measured the dependences of zeta potential on the pH for the MFPLL and Ab-MFPLL samples in PBS. As can be seen (Fig. 10) functionalized nanoparticles are stable in acidic medium up to pH = 6.

Additionally, taking into account the complexity of biological media, colloidal stability of both non-conjugated and Ab conjugated MFPLL were tested in 10% FBS DMEM cell culture media, at a magnetite concentration of 100 μg/mL. Briefly, 0.1 mL of the tested sample

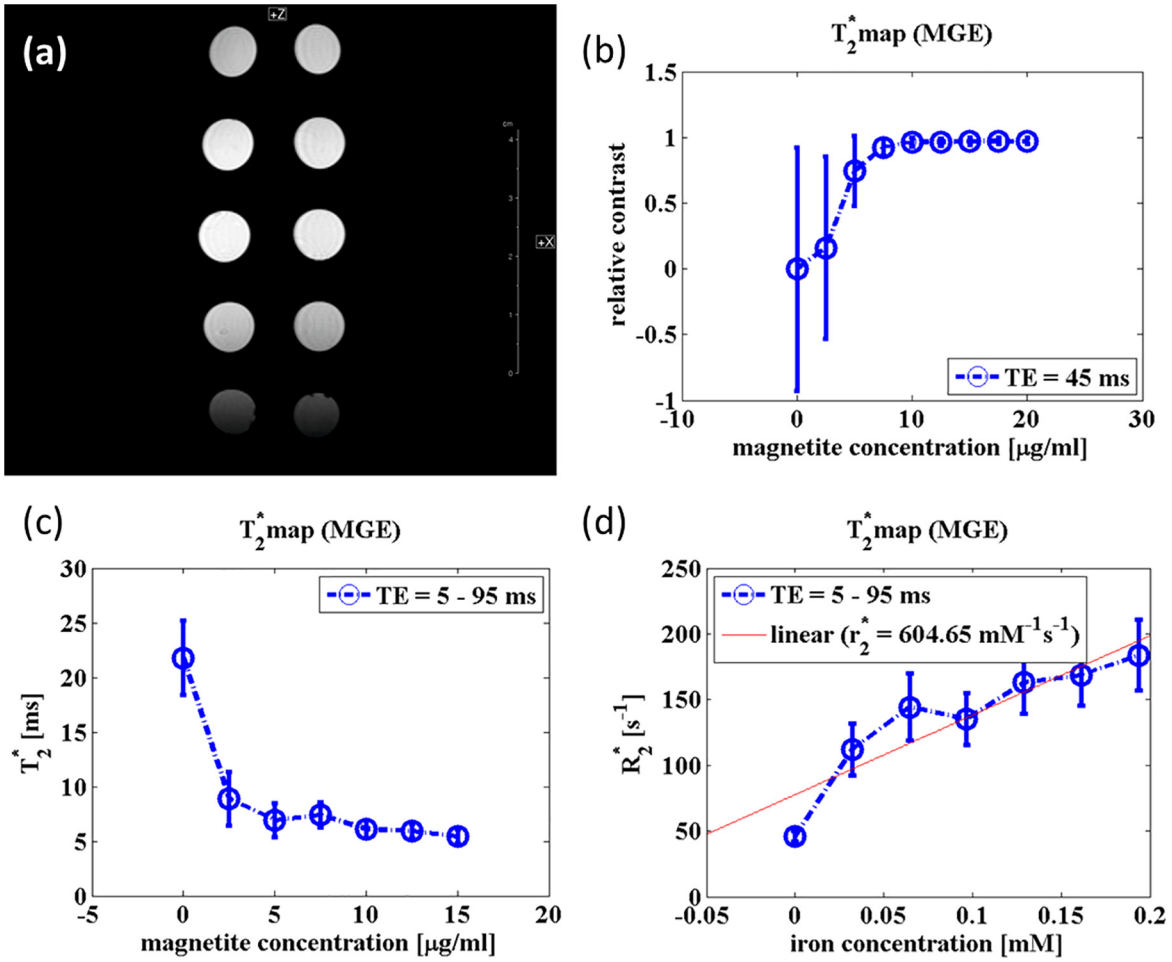

Fig. 9. Transversal relaxation time mapping of the poly-L-lysine modified magnetic nanoparticles with T_2^*-mapping MGE pulse sequence. (a) The signal intensity. (b) The relative contrast depending on the magnetite concentration. (c) The relaxation time T_2^* depending on the magnetite concentration. (d) The relaxation rate R_2^* depending on the magnetite concentration. Calculated relaxivity $r_2^* = 604.65\,\mathrm{mM^{-1}\,s^{-1}}$.

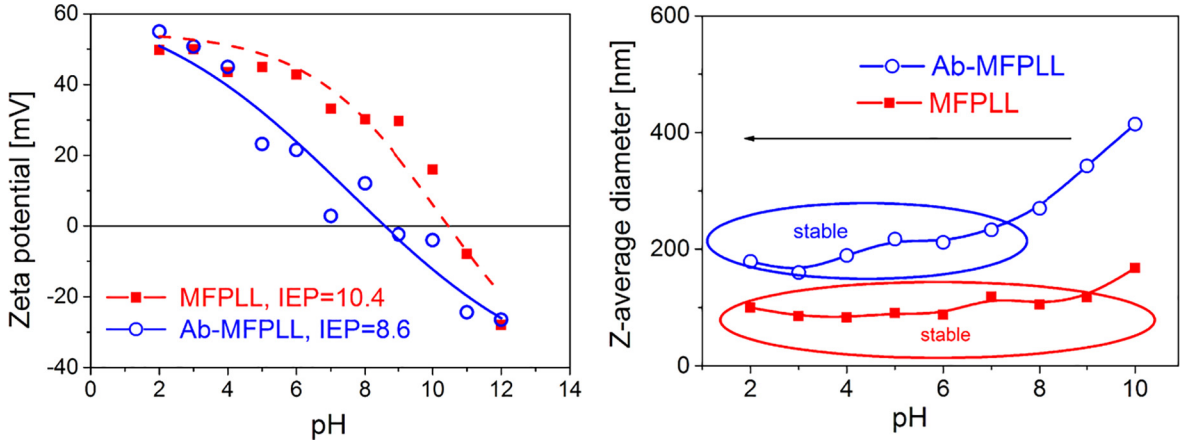

Fig. 10. pH dependence of Zeta potential (left) and Z-average diameter (right) of pure MFPLL and Ab-MFPLL in PBS.

was mixed with 0.9 mL 10% FBS DMEM cell culture media and incubated at 25 and 37 °C under mild shaking while time evolution of hydrodynamic size was recorded. While MFPLL showed an increase in size after 44 h at room temperature, the Ab-MFPLL sample remained stable, as D_{HYDR} showed no changes throughout the 74-hour measuring time. This is consistent with the polydispersity index measurements results (Fig. 11a–c). Similar behavior was observed at 37 °C. While non-conjugated samples were in a well-dispersed state all the way through the investigation time (Fig. 11b), Ab-conjugated samples showed a slight decrease in diameter (Fig. 11d). The behavior suggests that FBS could protect the nanoparticles from aggregating.

3.6. Cellular uptake study in 3D multicellular spheroidal cell culture

In vitro analyses of modified nanoparticles (MFPLL) conjugated to specific anti-CA IX VII/20 MAb were performed in 3D spheroids. Classic

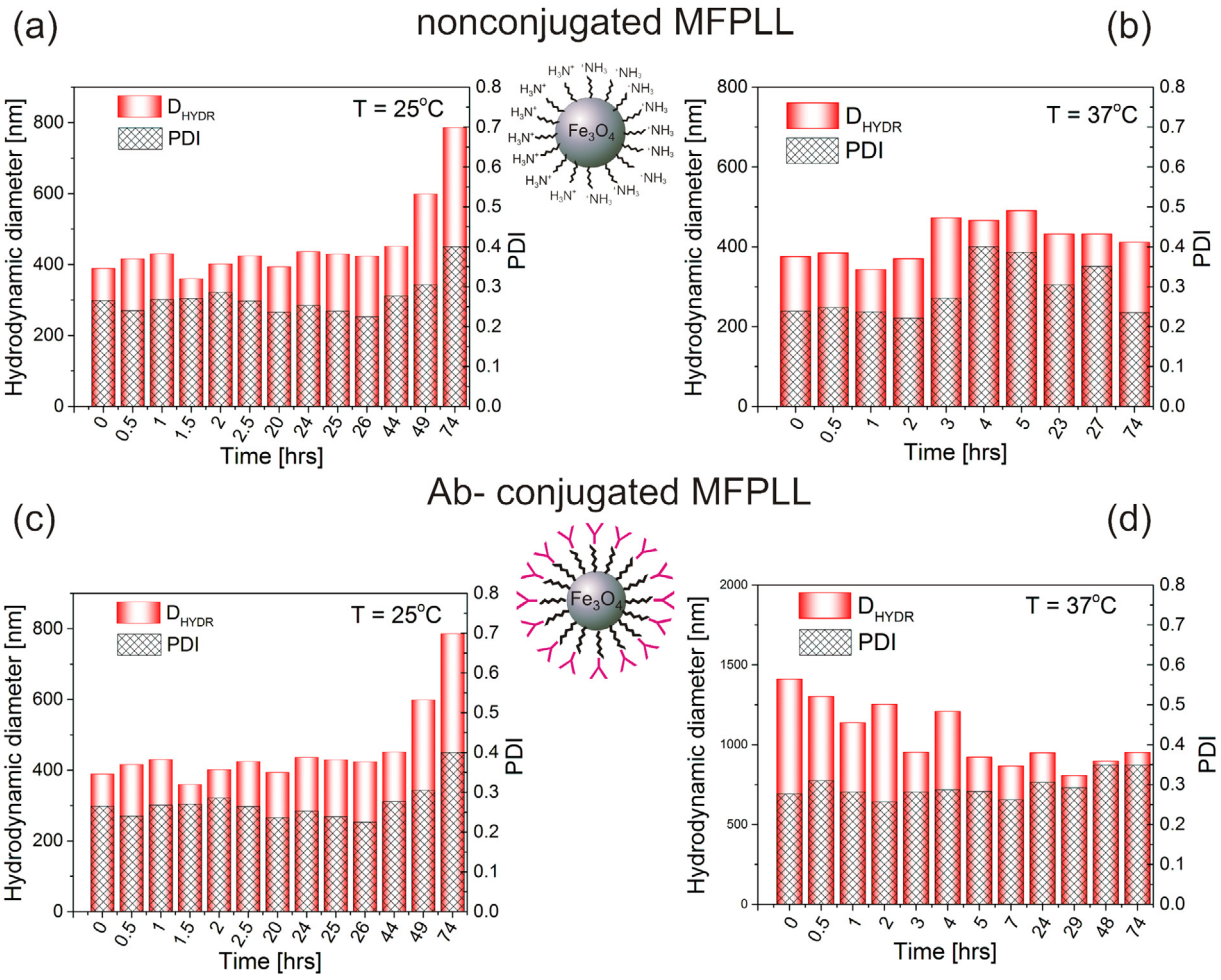

Fig. 11. Diameter and polydispersity index time dependences of the MFPLL (a,b) and Ab-MFPLL (c,d) as an indicator of samples' stability.

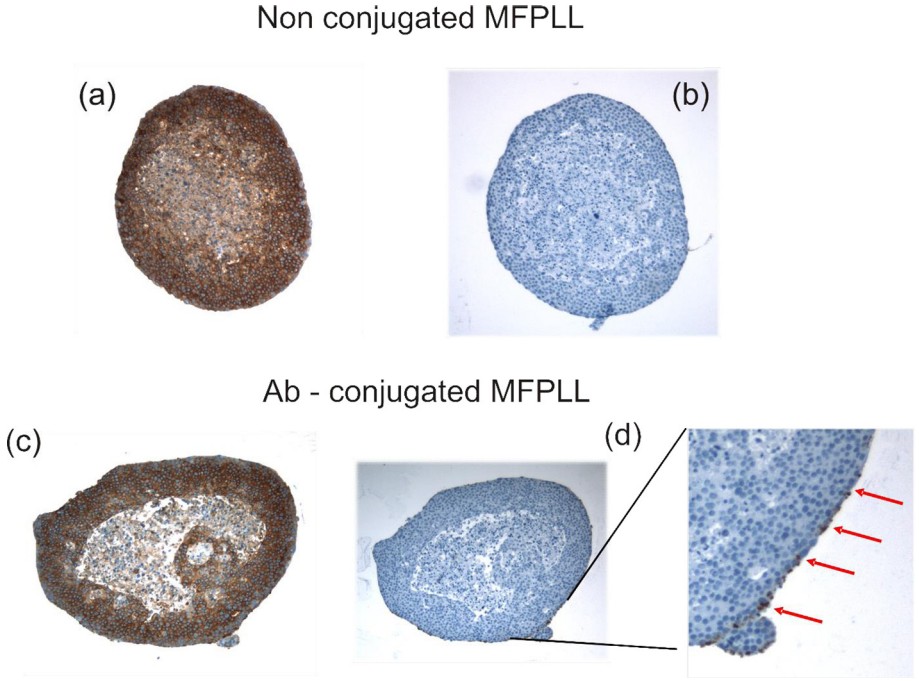

Fig. 12. Immunohistochemical staining of HT29 spheroid sections. Detection of CA IX protein using primary anti-CA IX monoclonal antibody M75 and secondary anti-mouse-HRP antibody in spheroids treated with non-conjugated MFPLL (a) and Ab-conjugated MFPLL (c). Binding of Ab-conjugated MFPLL (b) and non-conjugated MFPLL (d) respectively was detected using secondary anti-mouse-HRP antibody.

cell cultivation in monolayer strongly differs from real tumor, therefore, we used a model of multicellular spheroids that mimic tumor microenvironment more accurately. The spheroids were formed in hanging drops and cultivated in a Petri dish with the non-adherent surface for another 5 days. HT29 cancer cells are characterized by strong expression of CA IX and so they represent a suitable model for the analysis of specific binding of MFPLL-Ab conjugate. CA IX protein is localized on cell membranes and is recognized by specific monoclonal antibody VII/20.

Results of immunohistochemical analysis of paraffin-embedded sections of HT29 spheroids showed specific interaction of Ab-MFPLL conjugate and CA IX protein on cell membranes (Fig. 12d). This interaction was confirmed using secondary anti–mouse HRP conjugated antibody, which recognizes complex of Ab-MFPLL. In the spheroids treated with unconjugated MFPLL, the specific signal was missing (Fig. 12b). The presence of CA IX antigen for binding of Ab-MFPLL conjugate was confirmed using another specific anti-CA IX antibody M75, which recognizes a different domain of CA IX protein (Fig. 12a,c). Our results confirmed the interaction between Ab-MFPLL conjugate and CA IX protein. However, Ab-conjugated MNPs bound only to cells at the surface of the spheres. This is understandable since MNPs are much larger and more complex than the free antibody, penetration of which across several cellular layers requires time periods longer than 24 h. Moreover, penetration of molecules through 3D structures depends on the strength of cell-cell adhesions between HT29 cells that form very compact, tightly packed spheroids and are therefore poorly permeable via intercellular spaces. Also, internalization is compromised in tightly packed cells as demonstrated earlier [7]. We assume that binding of Ab-conjugated MNPs to directly accessible cells expressing CA IX is important and sufficient for targeting magnetic hyperthermia and potential destruction of CA IX-positive cells and consequently their bystanders. Nevertheless, this assumption requires further extensive experimentation using diverse cellular models and employing diverse magnetic hyperthermia treatment regimens.

4. Conclusion

In this study we aimed to verify the suitability of PLL-modified magnetic nanoparticles for magnetic hyperthermia and magnetic resonance imaging application. For this purpose, biocompatible amino modified magnetic nanoparticles were prepared and subsequently conjugated to specific antibody. The samples were subjected to a series of calorimetric measurements. Calculated SAR values (~14–15 W/g) at used conditions are comparable with results found in literature and suitable for the future study focusing on detection of tumor cells mediated by antibodies and on therapy in combination with MRI and hyperthermia. The combination represents a significant advance in cancer diseases treatment and a substantial improvement in survival of oncological patients. Of course, heating characteristics (ΔT, dT/dt, SAR) can be tailored by variation of experimental conditions such as frequency, field intensity or particles concentration and particles' parameters. The MRI parametric mapping showed the significantly prevailing effect of the PLL modified magnetic nanoparticles on the transversal relaxation time T_2 compared to longitudinal relaxation time T_1. Such stabilized nanoparticles have definitely potential as the MRI contrast agent in the proclaimed combination of biomedical applications. Moreover, their relaxivity value r_2 exceeds the transversal relaxivity of clinically used iron-based contrast agents. Our results confirmed specific binding of Ab-conjugated MFPLL to CA IX protein in 3D model of colorectal cancer cells. Previous results have shown antibody-induced receptor internalization properties of VII/20 MAb [7] which can be important for delivery of conjugates into tumor cells and for possible use of this conjugate in combined anticancer therapy.

Acknowledgements

This work was supported by the Slovak Research and Development Agency under the contracts No. APVV-14–0120, APVV-14–0932, APVV-15-0453 and APVV-14-0088, by the Ministry of Education Agency for Structural Funds of EU (Project ITMS 26220120033 and 26220220186), by the Slovak Scientific Grant Agency projects VEGA 2/0045/13, VEGA 2/0108/16, VEGA 2/0081/14 and VEGA 2/0133/16, by COST TD 1402 Radiomag, Biomedical Center Martin project (ITMS code: 26220220187, project co-financed from EU sources) and NanoCEXmat II (ITMS: 26220120035). The authors are grateful to Vladimir Girman (Pavol Jozef Safarik University, Kosice, Slovakia) for TEM measurements and analysis.

References

[1] B. Thiesen, A. Jordan, Clinical applications of magnetic nanoparticles for hyperthermia, Int. J. Hyperth. 24 (2008) 467–474, https://doi.org/10.1080/02656730802104757.
[2] C. Blanco-Andujar, A. Walter, G. Cotin, C. Bordeianu, D. Mertz, D. Felder-Flesch, S. Begin-Colin, Design of iron oxide-based nanoparticles for MRI and magnetic hyperthermia, Nanomedicine 11 (2016) 1889–1910, https://doi.org/10.2217/nnm-2016-5001.
[3] I. Khmara, M. Koneracka, M. Kubovcikova, V. Zavisova, I. Antal, K. Csach, P. Kopcansky, I. Vidlickova, L. Csaderova, S. Pastorekova, M. Zatovicova, Preparation of poly-L-lysine functionalized magnetic nanoparticles and their influence on viability of cancer cells, J. Magn. Magn. Mater. 427 (2017) 114–121, https://doi.org/10.1016/J.JMMM.2016.11.014.
[4] M. Zatovicova, L. Jelenska, A. Hulikova, P. Ditte, Z. Ditte, L. Csaderova, E. Svastova, W. Schmalix, V. Boettger, P. Bevan, J. Pastorek, S. Pastorekova, Monoclonal antibody G250 targeting CA IX: binding specificity, internalization and therapeutic effects in a non-renal cancer model, Int. J. Oncol. 45 (2014) 2455–2467, https://doi.org/10.3892/ijo.2014.2658.
[5] M. Zaťovičová, S. Pastoreková, Modulation of cell surface density of carbonic anhydrase IX by shedding of the ectodomain and endocytosis, Acta Virol. 57 (2013) 257–264, https://doi.org/10.4149/av_2013_02_257.
[6] M. Zat'ovicová, K. Tarábková, E. Svastová, A. Gibadulinová, V. Mucha, L. Jakubícková, Z. Biesová, M. Rafajová, M. Ortova Gut, S. Parkkila, A.K. Parkkila, A. Waheed, W.S. Sly, I. Horak, J. Pastorek, S. Pastoreková, Monoclonal antibodies generated in carbonic anhydrase IX-deficient mice recognize different domains of tumour-associated hypoxia-induced carbonic anhydrase IX, J. Immunol. Meth. 282 (2003) 117–134.
[7] M. Zatovicova, L. Jelenska, A. Hulikova, L. Csaderova, Z. Ditte, P. Ditte, T. Goliasova, J. Pastorek, S. Pastorekova, Carbonic anhydrase IX as an anticancer therapy target: preclinical evaluation of internalizing monoclonal antibody directed to catalytic domain, Curr. Pharm. Des. 16 (2010) 3255–3263 http://www.ncbi.nlm.nih.gov/pubmed/20819068.
[8] A. Skumiel, B. Leszczyński, M. Molcan, M. Timko, The comparison of magnetic circuits used in magnetic hyperthermia, J. Magn. Magn. Mater. 420 (2016) 177–184, https://doi.org/10.1016/j.jmmm.2016.07.018.
[9] M. Babič, D. Horák, M. Molčan, M. Timko, Heat generation of surface-modified magnetic γ -Fe $_{2}$ O 3 nanoparticles in applied alternating magnetic field, J. Phys. D. Appl. Phys. 50 (2017) 345002, , https://doi.org/10.1088/1361-6463/aa7bcb.
[10] I. Khmara, M. Kubovcikova, M. Koneracka, B. Kalska-Szostko, V. Zavisova, I. Antal, M. Rajnak, Z. Dankova, V. Kavecansky, M. Omastova, P. Kopcansky, Preparation and characterization of magnetic nanoparticles, Acta Phys. Pol. A. 133 (2018) 704–706, https://doi.org/10.12693/APhysPolA.133.704.
[11] M. Timko, M. Molcan, A. Hashim, A. Skumiel, M. Muller, H. Gojzewski, A. Jozefczak, J. Kovac, M. Rajnak, M. Makowski, P. Kopcansky, Hyperthermic effect in suspension of magnetosomes prepared by various methods, IEEE Trans. Magn. 49 (2013) 250–254, https://doi.org/10.1109/TMAG.2012.2224098.
[12] M. Molcan, H. Gojzewski, A. Skumiel, S. Dutz, J. Kovac, M. Kubovcikova, P. Kopcansky, L. Vekas, M. Timko, Energy losses in mechanically modified bacterial magnetosomes, J. Phys. D. Appl. Phys. 49 (2016) 365002, , https://doi.org/10.1088/0022-3727/49/36/365002.
[13] S. Dutz, R. Hergt, Magnetic nanoparticle heating and heat transfer on a microscale: basic principles, realities and physical limitations of hyperthermia for tumour therapy, Int. J. Hyperther. 29 (2013) 790–800, https://doi.org/10.3109/02656736.2013.822993.
[14] A. Skumiel, M. Kaczmarek-Klinowska, M. Timko, M. Molcan, M. Rajnak, Evaluation of power heat losses in multidomain iron particles under the influence of AC magnetic field in RF range, Int. J. Thermophys. 34 (2013) 655–666, https://doi.org/10.1007/s10765-012-1380-0.
[15] E. Illés, M. Szekeres, I.Y. Tóth, Á. Szabó, B. Iván, R. Turcu, L. Vékás, I. Zupkó, G. Jaics, E. Tombácz, Multifunctional PEG-carboxylate copolymer coated superparamagnetic iron oxide nanoparticles for biomedical application, J. Magn. Magn. Mater. 451 (2018) 710–720.
[16] Y.V. Kolen'ko, M. Bañobre-López, C. Rodríguez-Abreu, E. Carbó-Argibay, A. Sailsman, Y. Piñeiro-Redondo, M. Fátima Cerqueira, D.Y. Petrovykh, K. Kovnir, O.I. Lebedev, J. Rivas, Large-scale synthesis of colloidal Fe3O4 nanoparticles exhibiting high heating efficiency in magnetic hyperthermia, J. Phys. Chem. C 118

(16) (2014) 8691–8701.
[17] E.C. Rodrigues, M.A. Morales, S.N. de Medeiros, N.M. Suguihiro, E.M. Baggio-Saitovitch, Pluronic® coated sterically stabilized magnetite nanoparticles for hyperthermia applications, J. Magn. Magn. Mater. 416 (2016) 434–440.
[18] R. Hergt, S. Dutz, M. Röder, Effects of size distribution on hysteresis losses of magnetic nanoparticles for hyperthermia, J. Phys. Condens. Matter 20 (38) (2008) 385214.
[19] J. Estelrich, M.J. Sánchez-Martín, M.A. Busquets, Nanoparticles in magnetic resonance imaging: from simple to dual contrast agents, Int. J. Nanomed. 10 (2015) 1727–1741, https://doi.org/10.2147/IJN.S76501.
[20] Z.R. Stephen, F.M. Kievit, M. Zhang, Magnetite nanoparticles for medical MR imaging, Mater. Today (Kidlington) 14 (2011) 330–338, https://doi.org/10.1016/S1369-7021(11)70163-8.